INVESTIGATION OF BACKSCATTER X-RAY IMAGING TECHNIQUES FOR URANIUM DIOXIDE FUEL RODS

T. Jackson,[1] D. Hollenbach,[2] D. Shedlock[3]

[1] Department of Mechanical, Aerospace, and Nuclear Engineering, Rensselaer Polytechnic Institute, Troy, New York

[2] Oak Ridge National Laboratory, P.O. Box 2008, Oak Ridge, TN 37831-6170

[3] Nucsafe Inc., 601 Oak Ridge Turnpike, Oak Ridge, TN 37830

Abstract

Radiography by Selective Detection (RSD), was investigated for its ability to determine the presence and types of defects in a UO_2 fuel rod surrounded by zirconium cladding. Images created using a Monte Carlo model compared favorably with actual X-ray backscatter images from mock fuel rods. A fuel rod was modeled as a rectangular parallelepiped with zirconium cladding, and pencil beam X-ray sources of 160 kVp (79 keV avg) and 480 kVp (218 keV avg) were generated using the Monte Carlo N-Particle Transport Code to attempt to image void and palladium (Pd) defects in the interior and on the surface of the fuel pellet. It was found that the 160 kVp spectrum was unable to detect the presence of interior defects, whereas the 480 kVp spectrum detected them with both the standard and the RSD backscatter methods, though the RSD method was very inefficient. It was also found that both energy spectra were able to detect void and Pd defects on the surface using both imaging methods. Additionally, two mock fuel rods were imaged using a backscatter X-ray imaging system, one consisting of hafnium pellets in a Zircaloy-4 cladding and the other consisting of steel pellets in a Zircalloy-4 cladding which was then encased in a steel cladding (a double encapsulation configuration employed in irradiation and experiments). It was found that the system was capable of detecting individual HfO_2 pellets in a Zircaloy-4 cladding and may be capable of detecting individual steel pellets in the double-encapsulated sample. It is expected that the system would also be capable of detecting individual UO_2 pellets in a Zircaloy-4 cladding, though no UO_2 fuel rod was available for imaging.

Introduction

When a photon interacts with an atom, there are a variety of mechanisms for energy transfer from the photon to the atom. For low-energy photons (below 1.2 MeV), only two mechanisms have any real significance, the photoelectric effect and Compton scattering. In the photoelectric effect an incident photon transfers all its energy to an atomic electron cloud, which results in an electron being emitted and no photon being emitted from the atom. In Compton scattering, the photon transfers only a portion of its energy to an atomic electron and scatters at some angle to the original direction of travel, with some relative probability associated with each angular change, including back towards the original photon source. The equation that governs the angular distribution and thus relative probability for Compton scattering is known as the Klein-Nishina cross section [1], the angular distribution of which is shown in Figure 1.

As Figure 1 shows, as energy increases, the angular distribution of Compton scattering shows a clear forward bias (i.e., away from the source) with increased energy. This implies that despite the increased photon range for higher-energy photons and increased probability of Compton scattering in comparison to photoelectric interactions, the net result is that each scattering interaction is less efficient, with an increased ratio of scattering events resulting in scattering away from the detectors instead of toward the detectors, creating a balance between higher range and thus deeper depth penetration but lower efficiency per interaction. The probability is expressed in terms of the total linear attenuation coefficient (μ_t), with the probability of interacting and being exponentially attenuated increasing with increased μ_t and material thickness. Each interaction type has its own μ, such as μ_{pe} for photoelectric effect and μ_{cs} for Compton scattering. The linear attenuation coefficient typically has dimensions of cm^{-1}. The mass attenuation coefficient, μ/ρ, typically has units of cm^2/g. Radiography by Selective Detection (RSD) uses this behavior and collimated detectors to selectively detect photons whose scattering events are below a critical depth [3, 4]. In comparison to traditional X-ray imaging modalities, RSD does not require transmission through an entire object and thus is applicable when only one side of an object is available for testing or when the material is of sufficiently high μ that the probability of transmission is negligible and thus transmission radiography is inefficient. As a general rule, μ increases with increasing atomic number *(Z)* for solid materials,

and therefore transmission-based imaging modalities are highly inefficient for high-*Z* materials, such as uranium oxide (UO_2).

The critical depth of a collimated detector is defined as the minimum depth at which a photon whose direction of movement can undergo a single scattering reaction, scatter into the detector's active volume, and is given by trigonometric considerations involving collimator length, detector size, and detector position. The concept of critical depth for a collimated system is shown in Figure 2. In Figure 2, the material thickness has a depth of 1.6 cm from the surface of the material, which corresponds to the thickness of the fuel rod measured in the MCNP simulations. The critical depth is defined as the depth inside the material corresponding to the vertex of a right triangle consisting of a horizontal line segment from the furthest edge of the detector active area parallel to the material surface, a vertical line from the particle source, and the hypotenuse between the two lines contiguous to the bottom edge of the collimator.

Figure 2 demonstrates that photons that scatter above a critical depth dependent on detector position and collimator length are not detected by the detector, whereas photons that scatter below the critical depth are capable of being detected. The scattering interaction above the critical depth in the direction of the detector is shielded by the collimator, while the scattering event below the critical depth is not shielded and can be detected. As a result of creating a critical depth, single-interaction photons can be detected only if they do not interact prior to reaching the critical depth. The relative effects of the existence of defects and their locations relative to detector position are well understood [4] so are not explained here in detail. Therefore there are two important considerations when determining the suitability of a material for analysis by RSD: the numerical value of μ and the relative values of the individual photoelectric (absorption) and Compton scatter (scattering) attenuation coefficients. For energies below about 1 MeV, μ/ρ tends to decrease with increased photon energy, with the exception of large positive vertical shifts at specific energies (which depend on the material) due to the discrete binding energy of each electron shell (e.g., K-edge transition), as shown in Figure 3.

Figure 3 demonstrates the presence of edge transitions indicative of the photoelectric effect, and Compton scattering beginning as a minor effect but changing to the dominant mode of interaction at approximately 650 keV for UO_2, which is well above the energy ranges used for X-ray backscatter imaging. Higher-energy photons for the same material would be more likely

to result in scattering events, though as seen in Figure 1, each scattering event is less efficient in producing backscatter photons. Compton scattering is dominant in low-*Z* materials at lower energies than for high-*Z* materials until it is overtaken by increasing μ_{pe} relative to μ_{cs}, as seen in Figure 4. For an ideal material, μ_{cs} should be very high in comparison to μ_{pe}, and the value for μ must be low enough such that a large proportion of photons do not interact prior to the critical depth. These considerations make it clear that high-*Z* materials such as UO_2 are not ideal materials to image using either transmission X-ray imaging or RSD.

Figure 4, when considered alongside Figure 1, explains why most previously performed RSD research [2, 3] has focused on low-*Z* materials. Low-*Z* materials not only have significantly more Compton scattering at low energies but a greater proportion of scattering events that result in backscatter due to the low energies. High-*Z* materials such as UO_2 have not been studied rigorously for their suitability for analysis with backscatter methods.

There is a significant incentive to model and image both unirradiated and irradiated fuel rods to detect possible defects during the manufacturing process and damage and deformation during irradiation [7]. Defects can be characterized as either high-density or low-density defects [3], and any modeling method must be able to detect both types. Methods already exist to inspect the quality of fuel rods [8], but current methods either image the exterior of the pellet prior to its insertion into the cladding rod and the external rod (at best) or require the production of neutrons [9], an unreasonable method from a practical standpoint. Backscatter methods have been shown to be useful in defect analysis of low-*Z* materials and require a comparatively small apparatus. Therefore, it is important to not discount the possible application of RSD and backscatter imaging to fuel rod defect detection and characterization as a final quality assurance measure.

Methods and Materials

MCNP and Geometry

The Monte Carlo N-Particle Transport Code (MCNP) [10] is a general-purpose radiation transport code that was used to simulate a four-detector RSD system performing a raster scan of a fuel rod model. The RSD system was designed to represent an RSD system created and used at The University of Florida [3] consisting of four collimated, cylindrical NaI detectors (5.08 cm

diameter) centered around a pencil beam photon source of a continuous-energy X-ray spectrum. The lower surface of each detector was 5 cm above the top surface of the fuel rod representation, with collimation in test cases reaching critical depths of 0, 0.15, 0.3, and 0.45 cm, with each depth corresponding to defect features. The same simulations and analyses were done with a 160 kVp (79 keV avg) spectrum and a 480 kVp (218 keV avg) photon spectrum. A schematic of the system with full collimation is shown in Figure 5.

The fuel rod representation used was a natural enrichment UO_2 rectangular parallelepiped ($3 \times 3.77 \times 1.6$ cm) with zirconium cladding (0.05 cm) on the +*z* parallelepiped surface. This was done with the knowledge that backscatter radiography would be difficult to accomplish throughout the width of the rod and that rastering by rotating an actual fuel rod about its length axis would in effect create a rectangular parallelepiped. In addition, two rectangular parallelepiped voids of thickness 0.05 cm and depth of 0.6 cm (grooves) transverse the width (*y*-axis) of the rod, with the z_{max} of the voids equaling the z_{min} of the zirconium cladding in order to represent the small amount of spacing between fuel pellets in a fuel rod. A spherical void defect (Void) (0.3 cm diameter) and palladium (Pd) rectangular parallelepiped defect ($0.5 \times 0.3 \times 0.15$ cm) were both strategically placed in the fuel pellet so that the effects of each defect did not interfere with the effects of the other defect or with the grooves in the rod, both having z_{max} of 0.15 cm below the top surface of the zirconium cladding (referred to as deep). Palladium was chosen because it is a fission product of ^{235}U and is generally considered a high-*Z* element. Additionally, the simulation was attempted for both X-ray source energies with the defects moved along the *z*-axis such that z_{max} would correspond to the bottom of the zirconium cladding, or 0.05 cm below the top surface (referred to as shallow).

Imaging and Image Processing

Raw data was created by using a rastering method of moving both the source and detector array in 1 mm increments over a fuel rod image that included both a portion of the fuel rod unaffected by grooves or defects, and a portion with grooves and defects. A total of 1×10^7 source particles were used for each position along the rastering path. Tallies were scored when one of the particles crossed the bottom surface of a detector. The same rastering method and the same tallies were used for both a base uncollimated case and a collimated test case. In the uncollimated case, each collimator length was selected such that the lower edge was coplanar

with the bottom of the detector. In the collimated case, each collimator length was selected such that the critical depth corresponded to defect features in the "deep" case, specifically the top of both defects, bottom of the Pd defect, and bottom of the void defect. The collimator lengths that corresponded to the chosen critical depths were 4.52, 4.65, and 4.79 cm for the 0.15, 0.3, and 0.45 cm critical depths, respectively. One detector in all cases was left with a collimator length of 0 cm (uncollimated) in order to create a base case for depth analysis and to test the standard uncollimated backscatter imaging method.

To analyze the features of an image, specifically the presence and nature of a defect, the numeric results of each detector were normalized using Equation 1:

$$X_{norm} = \frac{X - X_{true}}{\sqrt{X_{true}}} \tag{1}$$

where X_{norm} is the normalized count, X is the detected count, and X_{true} is the average of the count over the area of the fuel rod unaffected by the presence of any defects or grooves (Base). X_{norm} can be interpreted as analogous to the idea of "signal versus background" commonly used. The base case is a selected area of the analyzed surface at each collimation length which is unaffected by defects or grooves for each detector. As a result, changes in the base case are solely a result of transmission through UO_2. The $\sqrt{X_{true}}$ term can be interpreted as the standard deviation of the measurement due to expected Poisson statistics. The Poisson statistical nature of radiation measurement results in a general guideline that measurements must be at least 2σ different to be statistically relevant, so Eq. 1 was used to determine whether a numeric shift was the result of statistical variation or the presence of a defect. With this method, the results from detectors with different critical depths can be contrasted despite the decrease in absolute value of the detected signal as the critical depth increases throughout the rod, since the relative change from a portion of the rod unaffected by defects changes throughout the thickness of the rod due to defects. Additionally, the relative contribution by a defect to a generated image can be determined in order to ascertain the nature of a defect from a single image. Specifically, a void defect differs from an absorption defect in that a void defect causes a bright "shadow" with proper collimation, in contrast to the dark "shadow" of an absorber or scattering material [5]. Numerical results were analyzed graphically and compared using ImageJ [11], an open-source image processing program. To partially isolate the contribution from a defect over the depth of the defect, we use

$$RC = T - B \,, \tag{2}$$

where RC is the relative change in counts, T is the normalized count from a detector with critical depth at the top (z_{max}) of the defect, and B is the normalized count from a detector with critical depth at the bottom (z_{min}) of the defect.

Preliminary Experimental Verification

In an attempt to experimentally verify the application of backscatter X-ray imaging to fuel rods, two mock fuel rods were imaged using the imaging device shown in Figure 6. The mock fuel rods imaged are shown in Figure 7.

The Scatter X-ray Imaging (SXI) device is owned and operated by Nucsafe [12], with all imaging done on their premises. The SXI system used four large surface area, plastic scintillator detectors and an X-ray tube with a maximum voltage of 160 kVp which was moved over the demonstration fuel rods. One fuel rod consisted of a short segment of HfO_2 pellets, bordered on both sides by a lower density material, encased in a Zircaloy-4 tube. The other consisted of stainless steel pellets encased in a Zircaloy-4 clad pin (with a hold down spring) further encased in a stainless steel tube (a typical double encapsulated design for test reactor irradiation). Imaging was done with 0.1 mm pitch, and resultant images were analyzed using ImageJ.

Results

MCNP Simulation—160 kVp Spectrum

The number of photons that entered the detector for the case of a 160 kVp spectrum and defects with Z_{max} being 0.15 cm below the top surface of the zirconium is shown in Table 1. Numbers are all averages for regions in which the source is directly over the specific area.

In the deep defect instance, there is no numerical distinction between the void, Pd defect, and the UO_2 itself. There is too much attenuation within the UO_2 for any relevant results in the case of deep defects. Relative changes in detector response due to defect presence are all insignificant compared to inherent statistical variation and thus were not calculated. In contrast, the z_{max} = 0.05 cm case clearly demonstrates that there is a change in detector output due to defect presence. For example, the Pd defect changes detector response by amounts ranging from 28 standard deviations to 61 standard deviations, with similar results for the void defect (32–51).

This change allows an image to be generated from the results, improving defect visualization, as shown in Figure 8.

Unfortunately, Figure 8 does not show any visible shadowing for the Pd defect, so it is not possible to characterize the Pd defect, though the Pd defect is clearly detected as a defect. The void defect is distinguishable as a void defect, though it is difficult; increased counts would be expected to improve the ability to characterize the void defect as well. However, the image does show the small spacing between fuel pellets and shows that both the void and Pd defects are detectable. The relative shift in detector output as a result of the void defect is smaller than that of the Pd defect, likely due to its smaller size and more spherical shape than the rectangular parallelepiped shape of the Pd defect. It is clear that the 160 kVp source simulation is capable of detecting the presence of surface defects of the defect sizes used.

MCNP Simulation—480 kVp Spectrum

The rastering process used for the 160 kVp spectrum was also used for the 480 kVp spectrum. Table 2 gives the number of counts recorded using a 480 kVp spectrum and provides similar information to that found in Table 1 for the 160 kVp spectrum.

In the deep defect case, the void defect systematically decreases the detector response but only by statistically insignificant changes (0.8–1.8 standard deviations). This is similar to its behavior for the Pd defect (0.1–2.3 standard deviations), which is statistically relevant only for the uncollimated case. It is suspected that the low relative change in detector response for the deep defect scenario is only a result of the small counts, so the same analysis was performed using 6×10^7 initial particles in comparison to the 1×10^7 originally used; the results are shown in Table 3. The shallow defect portion of Table 2 provides some interesting information. The uncollimated, simple backscatter method shows very large relative changes due to both defects. The Pd defect in all collimation lengths for the shallow case is easily detected, but the void defect varies in its ability to be detected, notably having only a 0.9 standard deviation shift for the 0.3 cm critical depth case. This implies that the RSD method is inefficient for the shallow defect case, but the uncollimated backscatter method is sufficient to detect the presence of a defect.

Table 3 shows similar behavior to Table 2, with the only major difference being the numerical increase in counts. The uncollimated detector is capable of detecting both the Pd and the void defect, while the collimated detectors are much less efficient in detection, particularly for the Pd defect, and do not provide statistically significant results. It appears that the change in photon attenuation as a result of the Pd defect is too small at high energies for efficient detection and analysis using the RSD method. This is not to say that the RSD method fails, and indeed the statistics did improve as one would expect, but the relative change in detector response is very small. Therefore, it is reasonable to conclude that the RSD method does work for fuel rod imaging, but it is highly inefficient. As expected, however, the uncollimated detector provides statistically significant results, implying that backscatter imaging without application of the RSD method is capable of detecting defect presence.

Figure 9 shows the images generated from both the deep defect and the shallow defect cases for high-energy photons. In contrast to Figure 8, Figure 9 shows superior results, which demonstrates the superior ability of the 480 kVp spectrum not only to detect defects but to characterize them. The deep defect case clearly shows the presence of the void defect in the bottom right, as expected. Furthermore, the void defect and the grooves within the rod demonstrate bright "shadows," indicating their nature as voids. Similar behavior is seen for the shallow defect case, though not as pronounced. Interestingly, the bright "shadow" is also seen for the Pd defect, suggesting that it, in comparison to UO_2, is a mild void defect.

Comparison Between Spectra

An important question for system optimization is the energy optimization for either shallow or deep defect responses. The comparison between the 160 kVp spectrum and the 480 kVp spectrum for the deep defect case is shown in Figure 10.

It appears from a quick glance that the 480 kVp spectrum is superior to the 160 kVp spectrum at detecting the presence of defects that are relatively deep within the fuel pellet. This is not surprising due to the increased range of the photons, and it would be expected that the same procedure at even deeper critical depths would provide better analysis of defect depth. Even with the 480 kVp spectrum, however, it is still impossible to distinguish the presence of a defect while maintaining statistical validity using a relatively small number of source particles,

although it is possible using a very large number of source particles. As a result it is reasonable to assume that while the 480 kVp spectrum is capable of detecting a defect that is relatively deep within a fuel rod, it is inefficient. The same process to compare the qualities of both systems in analyzing the "deep" case was used to compare both systems with regard to the "shallow" case, as shown in Figure 11.

Similarly to the deep defect situation, it appears that the 480 kVp spectrum is superior to the 160 kVp spectrum at detecting a defect. However, some behaviors were unexpected: neither energy spectrum appears particularly useful for detecting the void defect, and the 160 kVp and 480 kVp spectra do not exhibit the same behavior with regard to the Pd defect. It appears that at lower energies, such as those seen in the 160 kVp spectrum, the Pd defect behaves very much like an absorber, thus decreasing the counts, while at high energies the Pd defect is thin enough and with low enough attenuation coefficient to be treated as a void. An absorber would be expected to have a negative deviation throughout, as seen in the 160 kVp results, while a void would be expected to start negative due to additional exit attenuation (see [5]) but increase to positive throughout the defect thickness, as seen in the 480 kVp results. It is clear then that Pd is not a true absorber defect or scatter defect in relation to UO_2. In practical scenarios, to at least some extent many materials would be considered a void in comparison to UO_2 due to the relative density and attenuation inherent in UO_2. UO_2 not only is very dense, but its Z_{eff} (effective atomic number) is also very high in comparison to most commonly used materials, which explains the high attenuation of photons in UO_2. Further research into the nature of expected defects in UO_2 is needed in order to develop better simulations. It is notable that the numeric values of the deviation (-12.4 for the 160 kVp spectrum and -6.6 for the 480 kVp) signify that the system is capable of detecting the void defect, but probably because of the size difference, the system is superior in detecting the relatively large Pd defect. A larger void defect of the same geometry as the Pd defect would be expected to provide equally significant results.

Throughout each simulation, counts generally increased with increasing critical depth from 0.15 to 0.45 cm. While the increase in counts ranged from negligible to over 20%, much of the increase could be attributed to defect presence impacting the results in various ways (Pd acting as a void, etc.), so an increase within areas unaffected by defect presence is significantly more interesting, particularly since a decrease in counts is expected. The reasonable explanation

is that the specific location of each detector created preferential scattering towards locations that then scattered in the direction of the detector. The simulation process was not repeated with each detector having its critical depth changed, but if there were a significant change in counts, then the assumption would be verified that the locations of each detector resulted in the systematic increase in counts. Although not performed, changing which detectors correspond to which critical depth would verify the preferential scattering.

Results from SXI imaging

The numeric results from the SXI imaging process were converted with ImageJ into an image, which is shown in Figure 12. The upper fuel rod is composed of steel pellets inside a Zircaloy-4 clad encased in a steel rod, and the bottom fuel rod is composed of HfO_2 pellets inside a Zircaloy-4 rod. A number of distinguishing characteristics of both rods are readily apparent from the image. It is easy to differentiate between pellets in the HfO_2 rod and difficult to differentiate between pellets in the steel rod. One of the reasons for this is the chamfered ends of the HfO_2 pellets vs. the flat ends of the steel pellets. The lower density pellets bordering the HfO_2 pellets are readily visible, and it is possible to detect the spring and Zircaloy-4 pins and caps within the outer stainless steel cladding. However, there is a distinct difference in the relative ability of the system to distinguish the steel pellets from the steel cladding and the individual HfO_2 pellets from the Zircaloy cladding. The system creates a clear visual distinction between hafnium and Zircaloy, two materials of significantly different *Z* (and therefore electron density), and even is capable of distinguishing individual pellets. This is due to the chamfered ends of the HfO_2 pellets, which produce the equivalent of large void defects between pellets, as shown in Figure 12. This shows that significant void defects are easily identified using X-ray backscatter imaging. The same ease of distinction is not possible in the steel pellet and steel cladding case, however. It is possible, though not easy, to distinguish the pellets from the cladding, but the flat edges of the pellets render it impossible to discern between individual pellets with the resolution used in scanning. Decreasing the pixel size used in the scanning process would be expected to improve the image resolution and possibly allow for individual pellet differentiation in the steel rod. If the pellets were replaced with UO_2, as in an actual fuel rod, the ability of the system to detect individual pellets would be expected to have a similarly pronounced effect due to the similar difference in photon attenuation between Zircaloy and UO_2

and Zircaloy and HfO_2. While no experimental investigation was done on the system's ability to perform defect or depth analysis, it is capable of distinguishing a high-Z material from a low-Z and is capable of detecting individual pellets.

Conclusion

Compared with traditional methods of fuel rod imaging, backscatter X-ray imaging provides not only surface data about fuel pellets contained within zirconium cladding but also some degree of depth analysis without the need for a neutron source. A 160 kVp X-ray source was used to test the abilities of the radiography by selective detection (RSD) method for both deep defects and shallow defects, and the results were compared with those of a 480 kVp X-ray source by using Monte Carlo simulations. It was found that the deep defects (z_{max}= 0.15 cm below rod surface) were detectable only by the 480 kVp spectrum, though it was very inefficient in doing so when RSD (Radiography by Selective Detection) was used. The 160 kVp spectrum was capable of detecting both a Pd defect and a void defect in the shallow case (z_{max} = 0.05 cm below rod surface), but it exhibited some behavior inconsistent with the 480 kVp spectrum. Furthermore, all detectable defects were detected by the uncollimated detector, signifying that simple backscatter X-ray imaging does suffice for detection, though depth characterization requires the RSD method. More research is needed into energy optimization versus defect depth. A trade-off exists between increased photon penetration depth and efficiency loss due to increased forward scattering for higher-energy photon energy interactions.

References

[1] M. Weinberg. *The Quantum Theory of Fields*. (1995)

[2] S.M. Blinder. *Klein-Nishina Formula for Photon-Electron Scattering.* Web: Wolfram Demonstration Project website (20 July 2010)

[3] Benjamin T. Addicott. *Characterization and Optimization of Radiography by Selective Detection Backscatter X-Ray Imaging Modality.* Thesis. University of Florida (2006). Web: University of Florida website, at "Scatter X-ray Imaging"

[4] Daniel Shedlock. *X-Ray Backscatter Imaging for Radiography by Selective Detection and Snapshot: Evolution, Development, and Optimization.* Diss. University of Florida (2007). Web: University of Florida website, at "Scatter X-ray Imaging"

[5] *XMuDat: Photon Attenuation Data on PC.* Report. International Atomic Energy Agency (Aug. 1998). Web: IAEA website, 22 July 2010

[6] Oldenberg. *Modern Physics For Engineers*. McGraw-Hill, New York (1966)

[7] IAEA. *Computational Analysis of the Behaviour of Nuclear Fuel Under Steady State, Transient and Accident Conditions*. Rep. no. 1578. International Atomic Energy Agency (Dec. 2007). Web: IAEA website, 15 July 2010

[8]Raymond W. Brashier. *Method of Inspecting the Quality of Nuclear Fuel Rod Ends.* Westinghouse Electric Corp., assignee. Patent 4994232. (19 Feb. 1991)

[9] F. Groeschel. "Neutron Radiography of Irradiated Fuel Rod Segments at the SINQ: Loading, Transfer and Irradiation Concept." *Nuclear Instruments and Methods in Physics Research Section A: Accelerators, Spectrometers, Detectors and Associated Equipment* **424.1**, 215–20 (1999). Web: ScienceDirect, 15 July 2010

[10] J.F. Briesmeister, Ed. *MCNP—A General Monte CarloN-Particle Transport Code.* LANL Report LA-13709-M, Los Alamos National Laboratory, Los Alamos, NM (2000)

[11] ImageJ. NIH. Web: <http://rsbweb.nih.gov/ij/>.

[12] Nucsafe. Web: <www.nucsafe.com>.

FIGURES

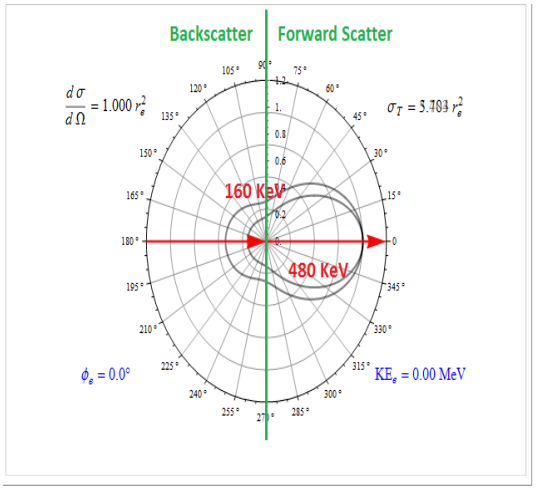

Figure 1: Free Electron Klein-Nishina cross-section angular distribution for 480 kVp and 160 kVp photons. Plot generated using Wolfram Mathematica [2].

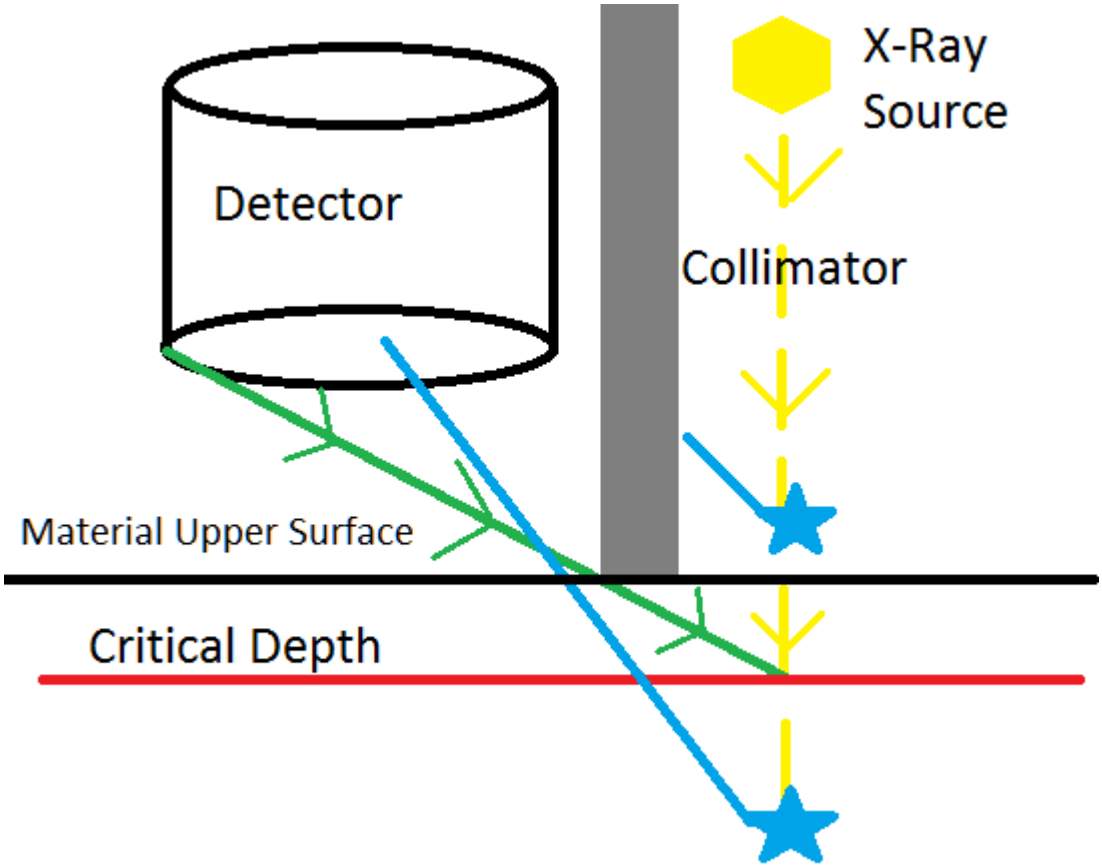

Figure 2: Pictorial representation of the concept of critical depth.

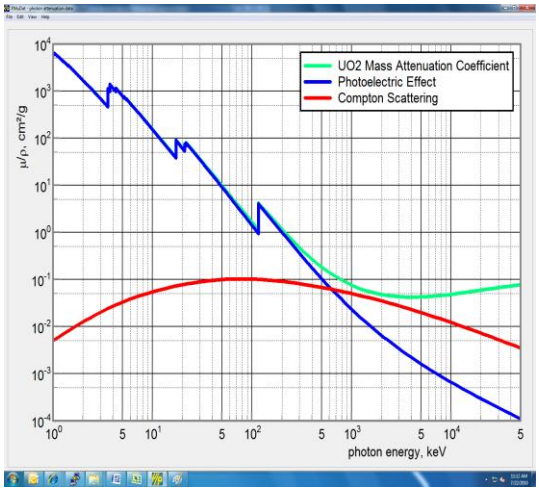

Figure 3: Mass attenuation coefficients for UO_2. Plot created in XMUDAT [5].

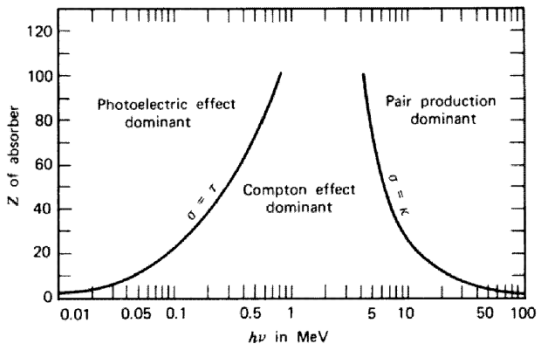

Figure 4: Dominant photon interaction type as a function of *Z* and photon energy [6].

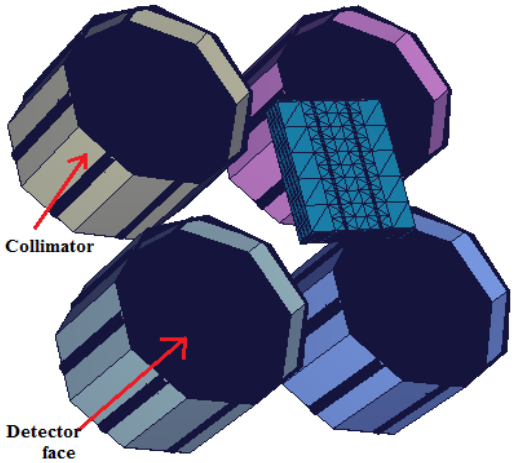

Figure 5: Fully collimated test case for backscatter system. The schematic was made with the MCNP Visual Editor.

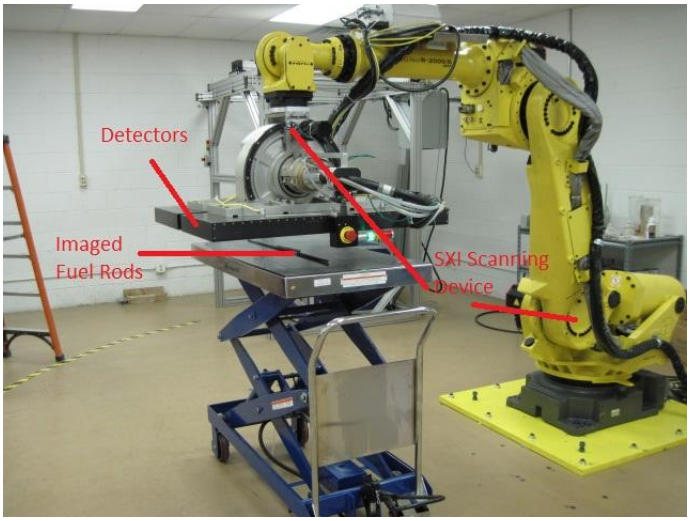

Figure 6: Imaging device used to visually inspect and verify mock-up fuel rods.

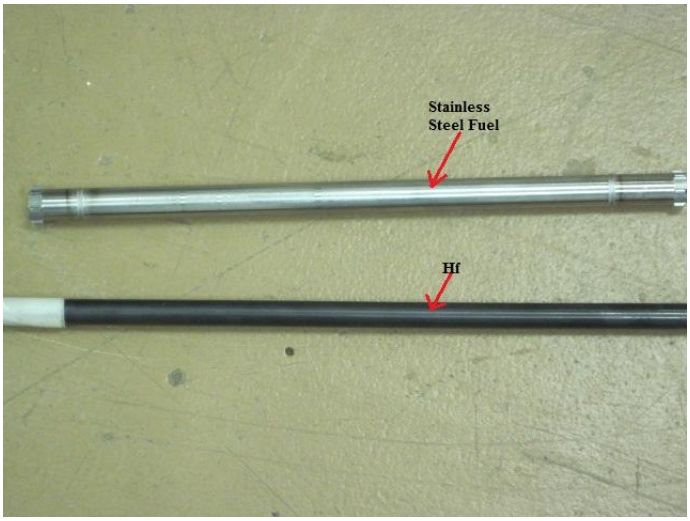

Figure 7: Mock fuel rods imaged using imaging device.

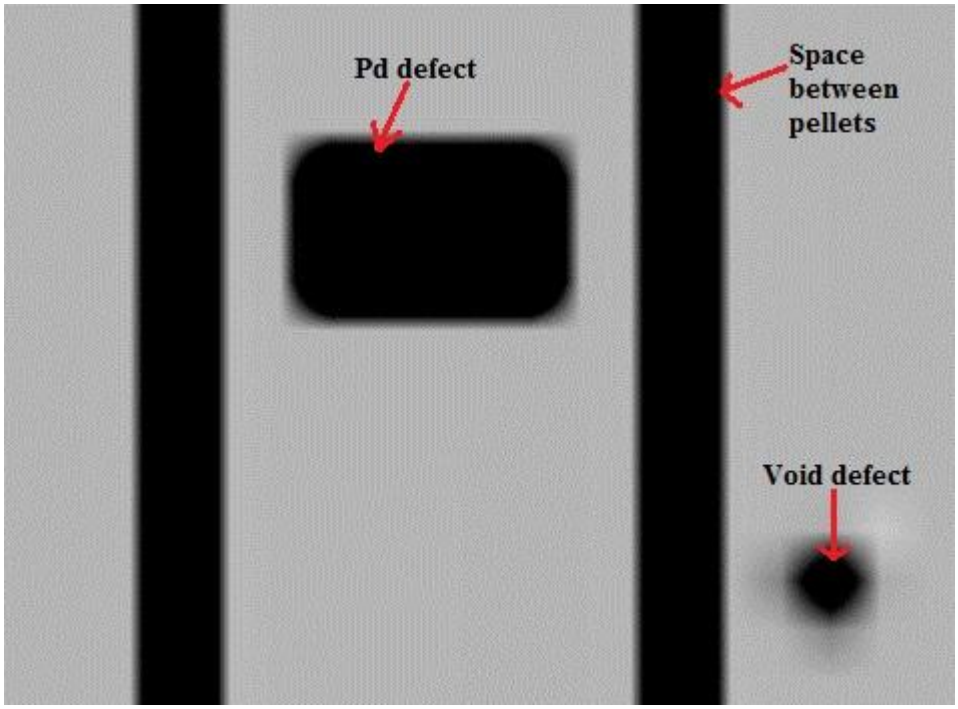

Figure 8: 160 kVp defects from 0.3 cm critical depth and shallow defect.

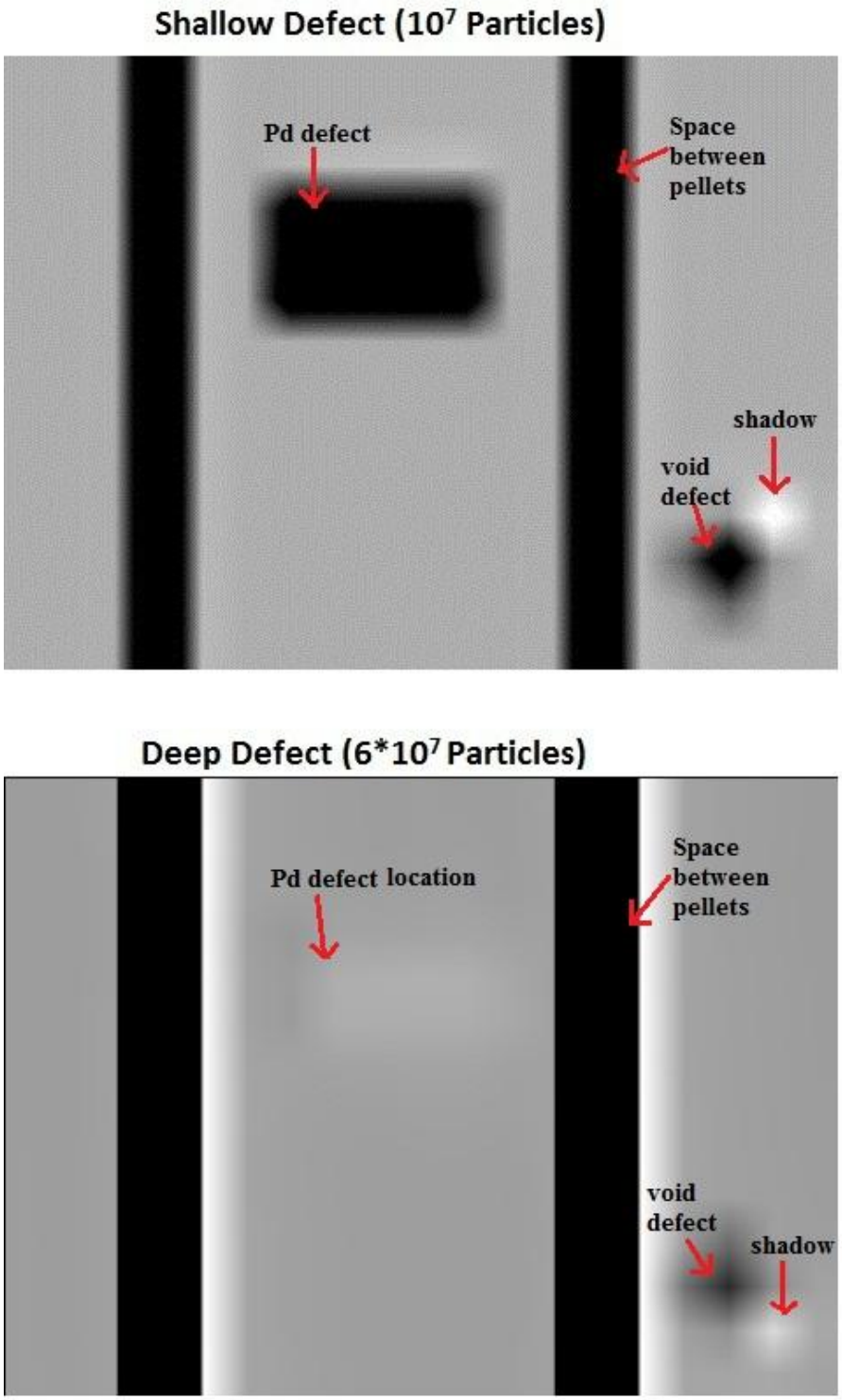

Figure 9: 480 kVp fuel rod image from uncollimated detector. Image generated in ImageJ.

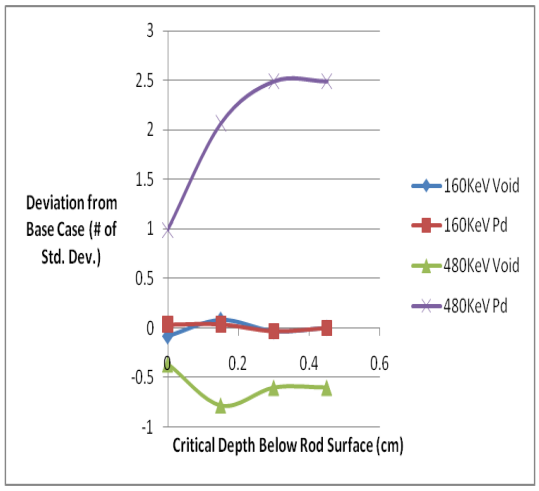

Figure 10: Deep defect comparison of spectra.

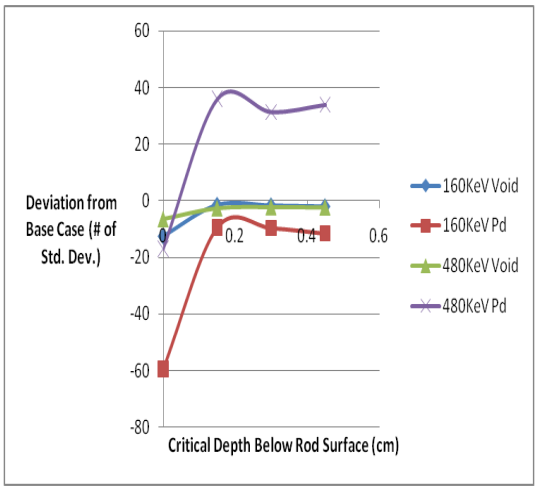

Figure 11: Shallow defect comparison of spectra.

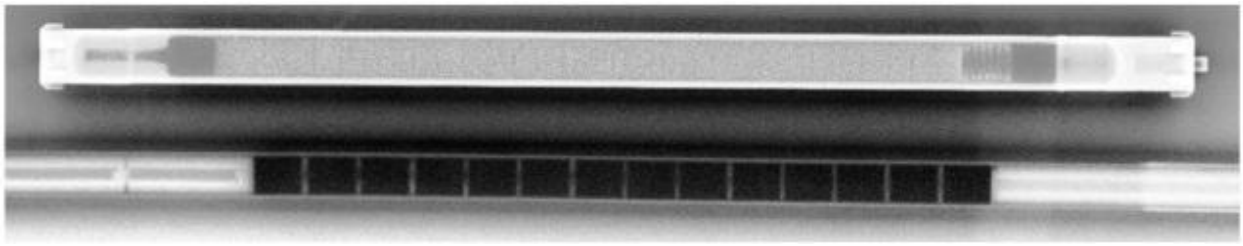

Figure 12: Fuel rods scanned with SXI.

TABLES

Table 1: Detector counts for the 160 kVp spectrum

Numerical values are actual tally values, (1×10^7 initial particles)

	Critical depth			
	0 cm (σ)	**0.15 cm (σ)**	**0.3 cm (σ)**	**0.45 cm (σ)**
Deep defects (z_{max}= 0.15 cm)				
Base	29760 (172)	1768 (42)	1917 (43)	2090 (45)
Void	29761 (172)	1768 (52)	1916 (43)	2090 (45)
Pd	29752 (172)	1768 (42)	1915 (43)	2088 (45)
Shallow defects (z_{max} = 0.05 cm)				
Base	29760 (172)	1768 (42)	1917 (43)	2089 (45)
Void	26146 (161)	1451 (38)	1509 (38)	1880 (43)
Pd	19070 (138)	528 (22)	662 (25)	684 (26)

Table 2: Detector counts for the 480 kVp spectrum

Numerical values are actual tally values, (1×10^7 initial particles)

	Critical depth			
	0 cm (σ)	**0.15 cm (σ)**	**0.3 cm (σ)**	**0.45 cm (σ)**
Deep defects (z_{max}= 0.15 cm)				
Base	38791 (196)	6223 (78)	6365 (79)	6585 (81)
Void	38421 (196)	6156 (78)	6297 (79)	6492 (80)
Pd	38323 (195)	6237 (78)	6251 (79)	6532 (80)
Shallow defects (z_{max} = 0.05 cm)				
Base	38791 (196)	6223 (78)	6365 (79)	6586 (81)
Void	32169 (179)	5358 (73)	5413 (73)	5708 (75)
Pd	24662 (157)	6608 (84)	6434 (80)	6752 (82)

Table 3: Detector counts for the 480 kVp spectrum, 6×10^7 particles

	Critical Depth			
	0 cm (σ)	**0.15 cm (σ)**	**0.3 cm (σ)**	**0.45 cm (σ)**
Deep defects (z_{max}= 0.15 cm)				
Base	232231 (481)	37573 (193)	38671 (196)	40093 (200)
Void	228703 (478)	37650 (194)	38548 (196)	39611 (199)
Pd	229898 (479)	37216 (192)	38226 (195)	40033 (200)